The International Journal of Advanced Manufacturing Technology (2018) 99:663–681
https://doi.org/10.1007/s00170-018-2521-9

ORIGINAL ARTICLE

Deformation characteristics and microstructural evolution in friction stir welding of thick 5083 aluminum alloy

Murshid Imam[1,2] · Yufeng Sun[3] · Hidetoshi Fujii[1] · Ninshu MA[1] · Seiichiro Tsutsumi[1] · Shuja Ahmed[2] · Viswanath Chintapenta[4] · Hidekazu Murakawa[1]

Received: 8 January 2018 / Accepted: 26 July 2018 / Published online: 8 August 2018

Abstract

The microstructure development in the weld key-hole along the plate thickness was investigated through scanning electron microscope (SEM), electron backscatter diffraction (EBSD), and transmission electron microscopy (TEM) techniques. A fundamental understanding of the contact condition at the tool/workpiece interface in a Triflat^{TM} designed friction stir welding (FSW) tool is presented. The development of grain structure for "stop-action" weld reveals that the plasticized material undergoes complex interacting flows due to the presence of threads and flats. The localized high material velocities induce a significant increase in the strain rate within thread space and thereby tune the Zener-Hollomon parameter. An interesting analogy is drawn between the evolution of the secondary shear zone (SSZ) in a typical metal cutting and the steady state FSW processes. The presence of different morphology of the material filling the thread space is linked to the local variation of the contact state variables along weld thickness. It was found that the contact state is governed by the intrinsic interface characteristics and the mechanical property of the material. It was also shown that the presence of larger particles ($> 0.5\ \mu$m) is responsible for the formation of high angle boundaries (HAGBs) and random recrystallization texture within the stir zone, reflecting random grain orientation due to particle-stimulated nucleation (PSN).

Keywords Friction stir welding · Particle-stimulated nucleation · Stop-action weld · Deformation state · Weld key-hole

1 Introduction

There has been growing interest in the welding industry in applying the solid-state welding benefits of friction stir welding (FSW) to join a thicker section of aluminum alloys [1, 2]. However, producing thick FSW section welds places additional demands on the FSW machine/tooling. The typical challenges that need to be addressed include (i) a large gradient in temperature between the top and the bottom of the weld leads to either an overheated shoulder influence region or insufficiently heated bottom region, (ii) the slower cooling rate, and (iii) the large stresses and the high temperatures leads to wear and failure of the FSW tool. Additionally, an adjustment in the process control parameters, such as tool rpm, welding speed, and forge axis load, is complex in the case of the thick section. At increased thickness, the requirement of larger forge axis load increases. The optimum heat balance can be achieved by the use of higher welding speed. But, it causes the larger stresses acting on the tool and hence leads to tool failure. In the present state of knowledge, simple to complex tool geometries are available in the market for the commercial success of the welding of aluminum and other soft alloys for sheet thickness less than 12 mm [3–11]. However, the tool design is still a hot topic to advance the practice of FSW in a plate thickness 20 mm or above [2, 12]. The development of new tool designs need to proceed with caution and experimental validations. Otherwise, flooding the heavy metal industries with many different complex design concepts with varying performances will produce the conflicting reports and

✉ Murshid Imam
murshid@iitp.ac.in

1 Joining and Welding Research Institute, Osaka University, Ibaraki, 5670047, Japan

2 Department of Mechanical Engineering, Indian Institute of Technology Patna, Patna, 801103, India

3 School of Materials Science and Engineering, Zhengzhou University, Zhengzhou 450001, People's Republic of China

4 Department of Mechanical and Aerospace Engineering, Indian Institute of Technology Hyderabad, Hyderabad, 502285, India

Table 1 Process parameters used in this work

Tool probe	Rotational speed (rpm)	Welding speed (mm/min)	Probe height (mm)	Axial load (kN)	Tool tilt angle (°)
Threaded Triflat ™ design	500	50	19.9	28	3

additional challenges for the adoption of FSW of thick aluminum welds. Aissani et al. [13] reported that the recent development of the Triflat^{TM} designed tool for the FSW of thick aluminum sections shows the superiority over the conventional cylindrical pin-type probe. However, in such tools, the contact state at the tool/workpiece interface is complex and numerically reproducing the conditions expected in the shear layer is extremely difficult. There is a wide agreement in the community that the lack of a reliable FSW model still not proposed to capture such a complex interface contact conditions [14]. For simplicity, the contact boundary conditions at the tool/workpiece are either considered as full sticking or tool geometries are reduced to simpler. In such models, the constitutive laws, such as Sellars and Tegart, Johnson-Cook, Buffa, Zhang and Chen, Heurtier, Arbegast, Saturated Hart model, etc., are chosen either because of availability of constants or ease of implementation. Kuykendall et al. [15] compared the accuracy of the different constitute laws keeping the processing condition same in friction stir welding of 5083 aluminum alloy. They reported that the constitutive laws alone could cause significant variation in the prediction of the processes responses, such as peak temperature, strain, and strain rates. Therefore, the present work is focused on the fundamental understanding of the in situ deformation state, which is ignored in the earlier reported works.

Furthermore, the microstructure which develops in stir zone (SZ) because of deformation condition at the tool/workpiece interface is highly sensitive to process responses, such as peak temperature, cooling rate, strain, and strain rate. Nandan et al. [4] reported that under the proper control conditions, the microstructure can be refined to equiaxed fine or ultrafine grains with high-angle boundaries (HAGBs) misorientation, which can present the ideal condition for improving the formability of the welded sheet. In particular, Garcia-Bernal et al. [16] and Chen et al. [17] reported that the fine recrystallized microstructure during FSW of 5083 AA renders such alloy with good formability and also suitable for superplastic forming. Imam et al. [18] reported that the dynamic recrystallization has been cited as the main mechanism to describe the formation of SZ microstructure in majority of the aluminum alloys containing fine second-phase particles. However, McNelley et al. [19] suggested that if the particle size is larger than 0.5 μm, these particles are intended to become sites for particle-stimulated nucleation (PSN) of recrystallization. Resulting recrystallization textures tend to be random, reflecting random grain orientations due to PSN [19–23]. Therefore, the aim of this work is to study the role of second-phase particles in the development of SZ microstructure. The material investigated in this study is 5083 AA, which in particular useful for superplastic forming interest because of its corrosion resistance, weldability and high strength to weight ratio. A "stop-action" weld is prepared with the probe in place for a better understanding of the microstructural evolution around tool probe. Also, the microstructural studies are made in the weld key-hole cross-section, which contains the information regarding the effect of tool geometry on the deformation state. Therefore, another important aim of this study is to provide the fundamental understanding of the complexity of the nature of contact state that occurs at the tool/workpiece interface. A framework is proposed based on an analogy between the FSW and the metal cutting processes. Having in mind that this work will provide the basis for the development of the reliable FSW models with the appropriate constitutive law, and allow researchers to evaluate the changes in the present tool design, operating parameters and possibly suggests new improvements to the process.

2 Experimental work

A recently developed Triflat^{TM} FSW tool was used for the joining of a 20-mm thick 5083-O aluminum alloy plate (Perrett et al. [2]). The process parameters used in the present study are listed in Table 1. The chemical composition of the work material is listed in Table 2. The samples for the microstructural analysis were prepared from weld key-hole cross-section perpendicular to the welding direction (WD). To analyze the presence of defects and

Table 2 Chemical compositions of 5083-O aluminum alloy

Element	Si	Fe	Cu	Mn	Mg	Cr	Zn	Ti	Al
Weight %	0.13	0.26	0.04	0.65	4.30	0.11	0.01	0.02	Bal

shape of the SZ, a weld key-hole cross-section was etched with Keller's reagent (150 ml H_2O, 3 ml HNO_3, 6 ml HF, and 6 ml HCL) for approximately 60 s to reveal the weld macrostructure. To study the effect of geometrical features of the tool, a "stop-action" weld is prepared in which the probe was broken when the tool was allowed to stop suddenly during the welding. The electron backscatter diffraction (EBSD) analysis was conducted using a JSM-7001FA field emission type scanning electron microscope (FE-SEM) operated at 25 kV. A step size of 0.7 μm was used for the EBSD scans. The specimens for the EBSD studies were electrolytically polished in a solution of 25% nitric acid in ethanol. To study the distribution and size of second-phase particles, transmission electron microscopy (TEM) investigation was performed using a JEOL 2010TEM operated at 200 kV on the samples taken from shear layer S1 region (see Fig. 12c). The TEM specimen was polished using Strurer's Tenupol-2 twin-jet electro-polisher system with a mixture of 30% HNO_3 and 70% CH_3OH at −30 °C. Microhardness measurements were taken using a Vicker's microhardness tester at 100 gf and 15 s dwell time. The samples for uniaxial tests were prepared as per ASTM: E8-M11 guidelines. Uniaxial tests were conducted at room temperature and a fixed cross-head speed of 1.2 mm/min.

3 Results and discussion

In FSW, the overall microstructure development is location sensitive. The final microstructure which develops in the weld cross-section undergoes successive stages during FSW. The schematic shown in Fig. 1a, provides an overall idea of the different stages in the microstructural development during FSW. To show the variations in the peak temperatures and strain along the longitudinal cross-section of the weld, the process was modeled using a commercial FEA code—DEFORM 3D software. A Lagrangian implicit code designed for metal forming processes was used to model the FSW process. The workpiece was modeled as a viscoplastic

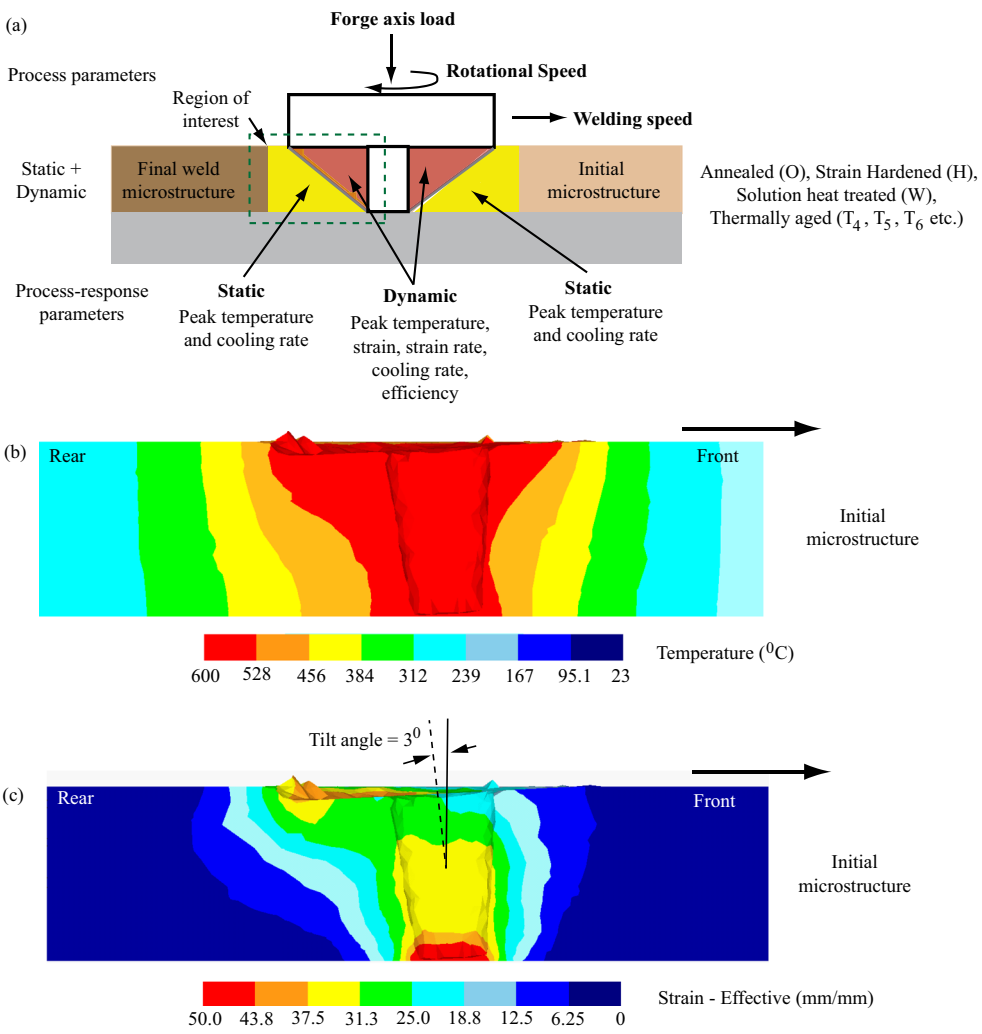

Fig. 1 **a** Schematic illustration of the microstructure development in different stages, **b** temperatures, and **c** strain distributions in longitudinal weld cross-section during FSW process

body and the welding tool was assumed rigid. For modeling the workpiece, 100000 tetrahedral elements were used and fine meshing was adopted at the tool/workpiece interface. In order to prevent distortion, an adaptive re-meshing technique was used. The degree of freedom of workpiece was restrained from all sides to take care of the clamping present during actual experiment. The viscoplastic behavior was modeled by the Johnson-Cook law [15, 24].

$$\overline{\sigma} = \left(A + B\bar{\epsilon}^{n}\right)\left(1 + C\ln\left(\frac{\dot{\bar{\epsilon}}}{\dot{\bar{\epsilon}}_0}\right)\right)\left(\frac{\dot{\bar{\epsilon}}}{\dot{\bar{\epsilon}}_0}\right)^{\phi}\left(D - \mathrm{ET}^{*m}\right) \quad (1)$$

Where, $T^* = (T\text{-}T_r)/(T_m\text{-}T_r)$ and $D = D_0 \exp[k(T\text{-}T_b)^{\beta}]$. Note that $A, B, n, C, \phi, \dot{\bar{\epsilon}}_0, D_0, k, \beta$ are model coefficients, T and m characterize the thermal softening of the material, T_r is the reference or room temperature, and T_m is the melting temperature. A thermal conductivity k = 180 N/s °C and thermal capacity of 2.4 N/mm^2 °C was used. The convection boundary condition was applied to the tool and workpiece surfaces exposed to the atmosphere. The heat exchange between workpiece and backing plate and between tool and workpiece was given a constant interface coefficient of 1.5 N/s mm °C. A constant shear friction factor of 0.3 was used for the tool/workpiece interface. The process parameters used in the simulation were identical to the actual welding condition. As illustrated in Fig. 1b, it can be seen that initial microstructure is subjected to a temperature in the range of 312–456 °C before it undergoes deformation. Generally, aluminum alloys are highly sensitive in this temperature range, change of microstructures, such as variations in precipitate morphology, grain size, grain boundary misorientation distribution, and crystallographic textures are expected. Based on this observation, it can be understood that initial base metal microstructure changes before deformation. The microstructure developed during the deformation stage is believed to change again because of post stirring annealing effect. Therefore, the final microstructure developed in the SZ is the combination of both the dynamic and static phases in FSW process. In addition, as illustrated in Fig. 1c, the strain distribution is more confined near to the probe in front of the tool. There is an initial deformation zone ahead of the tool probe and a highly deformed region closer to the tool probe/workpiece region. The highly deformed material moves to the back of the probe forming the SZ microstructure [25]. Note that here longitudinal cut section is shown in Fig. 1a–c during the FSW process. The tool tilting plays an important role in the distribution of temperature and plastic strain. The significant effect can be observed on the leading and trailing sides of the longitudinal section of the weld (see Fig. 1b, c). It is believed that the increase of peak temperature and larger compressive force on the trailing side of the tool causes more thermal softening and deformation of the material. Consequently, the material flow significantly improved on the trailing side of the tool, and hence, the formation of a defect like a wormhole can be avoided. It should, however, be noted that three different ways of microstructural studies could be performed in the FSW process, as shown in Fig. 2. In particular, most of earlier reported works, microstructure studies have been obtained from postmortem studies of completed welds (see Fig. 2a). The major drawback of this mode of microstructural studies that it does not provide the insight details of the grain structure development as the material interacts with and flows around the tool. The

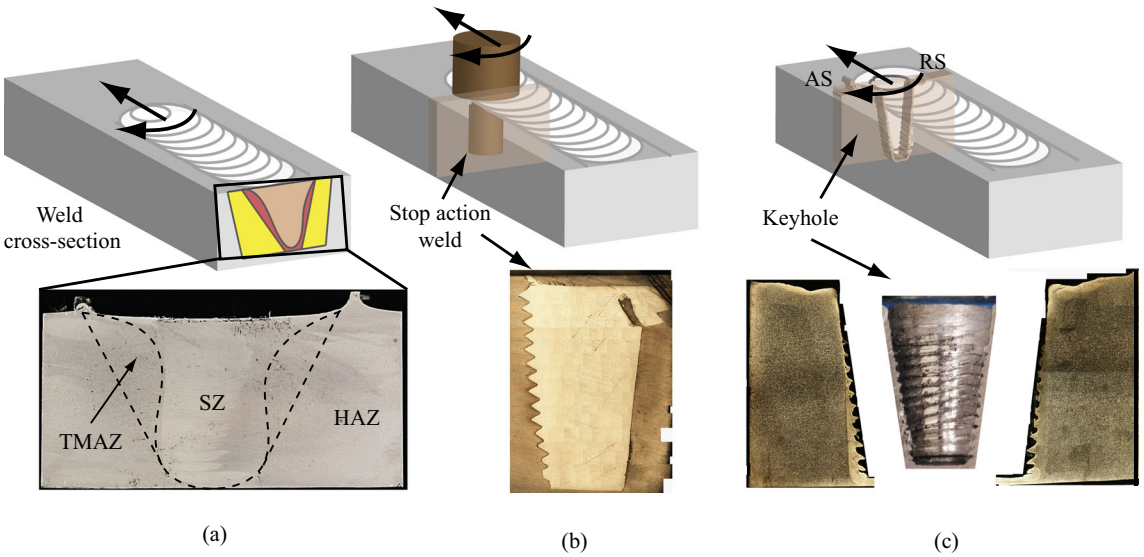

Fig. 2 Optical macrographs of **a** weld cross-section, **b** "stop-action" weld, and **c** weld key-hole considered for the microstructural study in the present case

"stop-action" welds technique, where the microstructure is allowed to freeze with the tool in place clearly shows the effect of tool geometrical features on the microstructural development (see Fig. 2b). Interestingly, the weld keyhole is not given proper attention despite it contains the information regarding the contact state variables, which directly dictates the intrinsic interface characteristics and the mechanical property of the workpiece material (see Fig. 2c).

Hardness profiles at three different depths for complete weld are shown in Fig. 3. The hardness profiles across the weld cross-section are almost identical at the three different depths. Note that in the case of solid solution hardened aluminum alloys, the hardness profiles was found to be strongly affected by the distribution of second phase particles, dislocation density and the dislocation/particle interaction which is commonly known as "Orowan hardening" [26, 27]. It is believed that the distribution of these second-phase particles does not varies significantly along the depth of the weld. It could be the reason for the hardness distributions along depth of the weld without much variations. The second-phase particles is believed to derive the strength by Orowan hardening, which is expressed by the following equation [27]:

$$\tau_y = \frac{Gb}{L} \tag{2}$$

where τ_y is the critical resolved shear stress, G is the shear modulus, b is the Burgers vector, and L is the average distance between particles. Generally, for aluminum alloys, the shear modulus and burger vector values are roughly 26000 MPa and 2.86×10^{-7} mm. In the above equation, the value of L is calculated by the following equation [27],

$$L = \sqrt{\frac{2\pi}{3f_v}} \times r \tag{3}$$

where f_v is the volume fraction of small particles and r is the radius of the small particles, which in the present case is $\frac{d_{avg}}{2}$. The calculated values of L and τ is shown in Fig. 3b (for details see the work reported by Imam et. al. [18]). Cahoon et al. [28] reported that the relationship between τ_y and yield stress is $\sigma_y = \sqrt{3}\tau_y$ and hardness is Hv = 3 σ_y for fcc materials. By using these relationships, the calculated value of hardness contributed by the

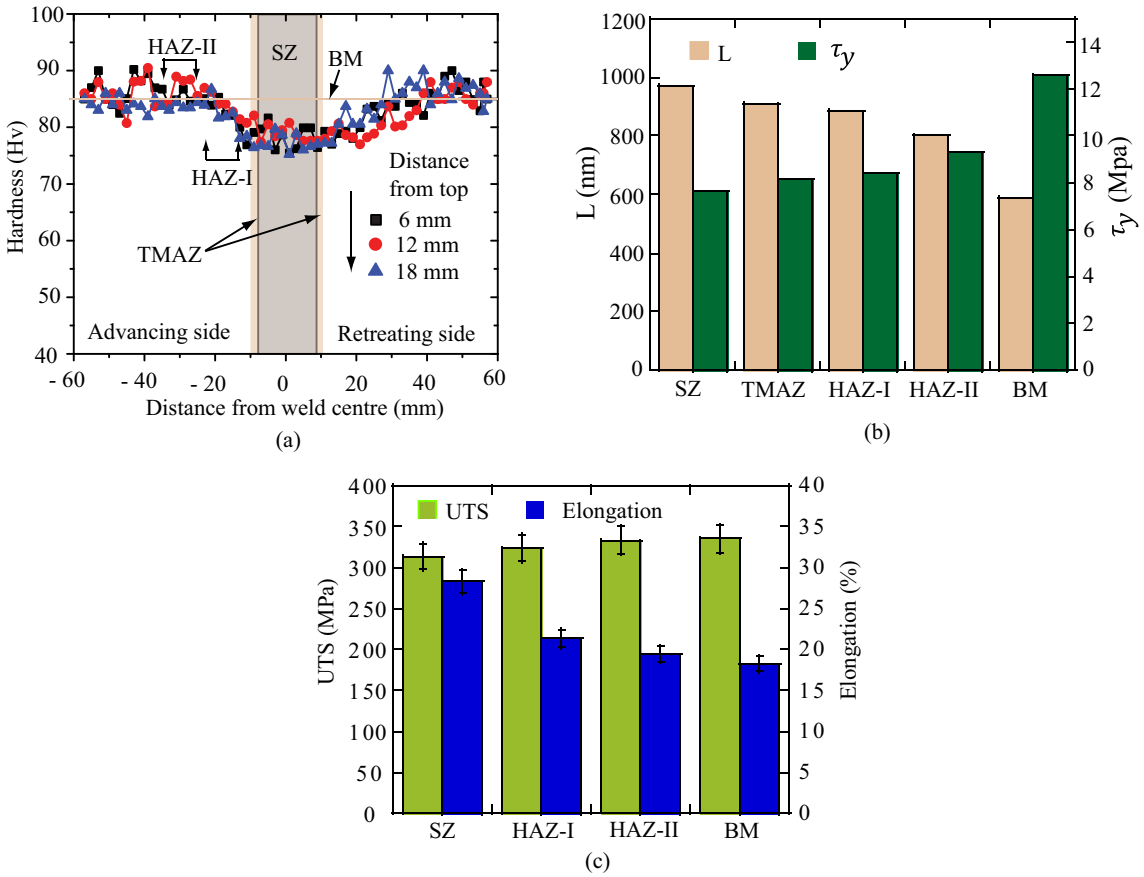

Fig. 3 Vicker's microhardness distributions at three depths [18], **b** calculated Orowan hardening parameters, and **c** comparison of ultimate tensile strength (UTS) and % elongation of different weld regions

small particles in SZ is 7.13 Hv. In addition, the variation in terms of ultimate tensile strength (UTS) and % elongation of different weld regions is shown in Fig. 3c. It can be seen that the ultimate tensile strength in SZ is slightly less than other weld regions and the base metal, while percentage elongation is significantly higher in this region. To obtain more details about the distribution of second-phase particles and dislocation density in the different weld regions, the TEM images are shown in Fig. 4. It can be clearly seen that the SZ is characterized by the presence of both large and small second-phase particles (see Fig. 4a). Further, the size and distribution of second-phase particles significantly varies from SZ to BM regions (see Fig. 4a-e). Note that the second-phase particles are $Al_6(Mn,Fe)$ type

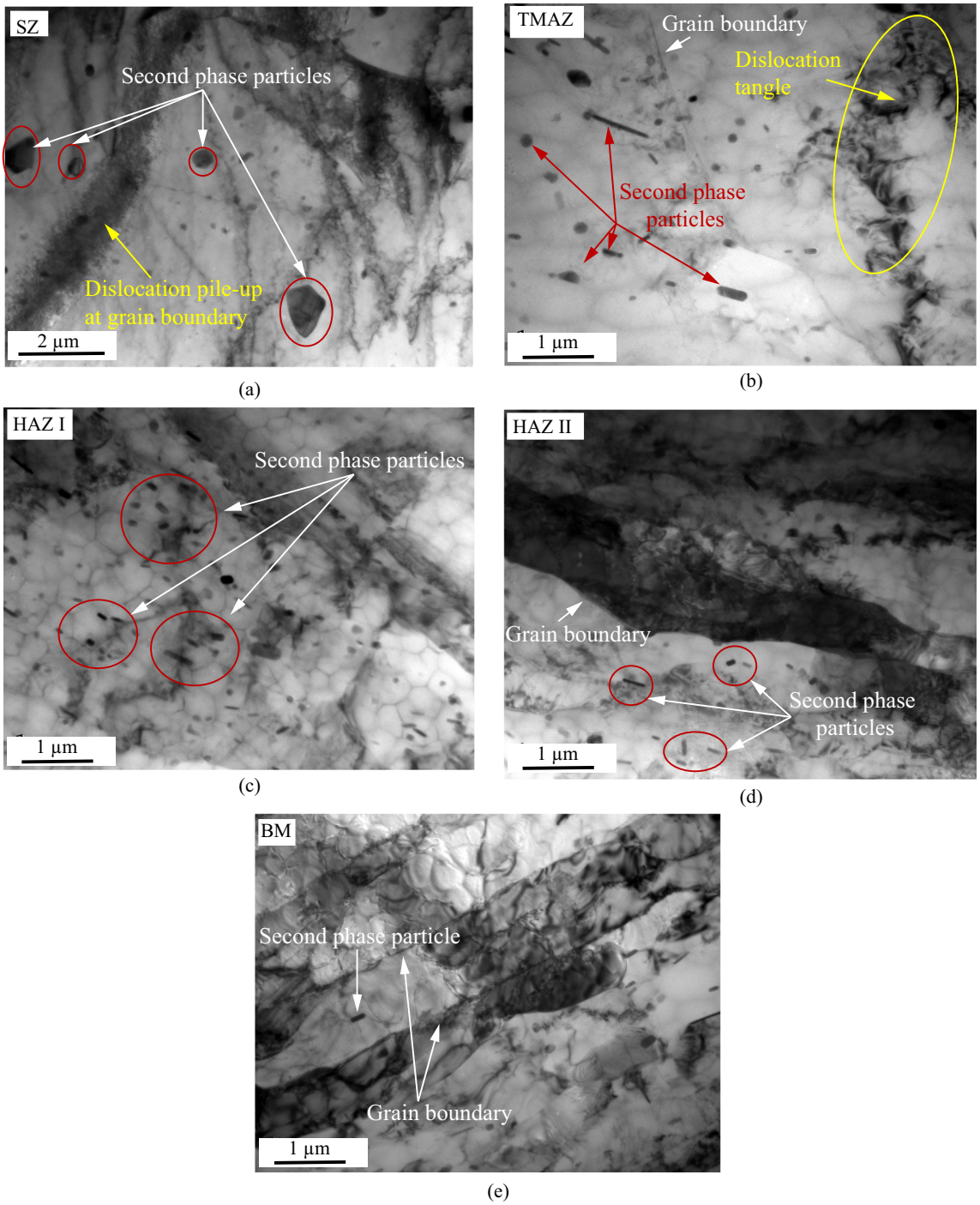

Fig. 4 **a**–**e** Transmission electron microscopy (TEM) images obtained from different weld regions and base material (BM)

with an orthorhombic crystallographic structure (for details, see the work reported by Imam et. al. [18]). Furthermore, no significant differences in the dislocation densities are observed between the HAZ-I and HAZ-II. However, the HAZ-I can be distinguished from HAZ-II on the basis of the distribution and size of the second-phase particles. In addition, The EBSD orientation color maps and corresponding crystallographic textures taken from HAZ and SZ are shown in Fig. 5a–d. In HAZ, the elongated grain morphology with typical rolling texture is observed (see also Fig. 12 for details on rolling texture components). The stir zone is characterized by the presence of equiaxed grain morphology with a weak recrystallization texture. Moreover, the weakening of recrystallization texture can be linked with the presence of second-phase particles. The presence of deformed second-phase particles can drastically alter the recrystallization behavior through a combination of PSN and Zener drag on the grain boundaries [29, 30]. When these particles have sufficiently larger size ($> 0.5\ \mu$m), they can store energy locally and accelerates the formation of nuclei for recrystallization [29, 31]. If the nuclei are sufficiently close together then grain growth does not occur

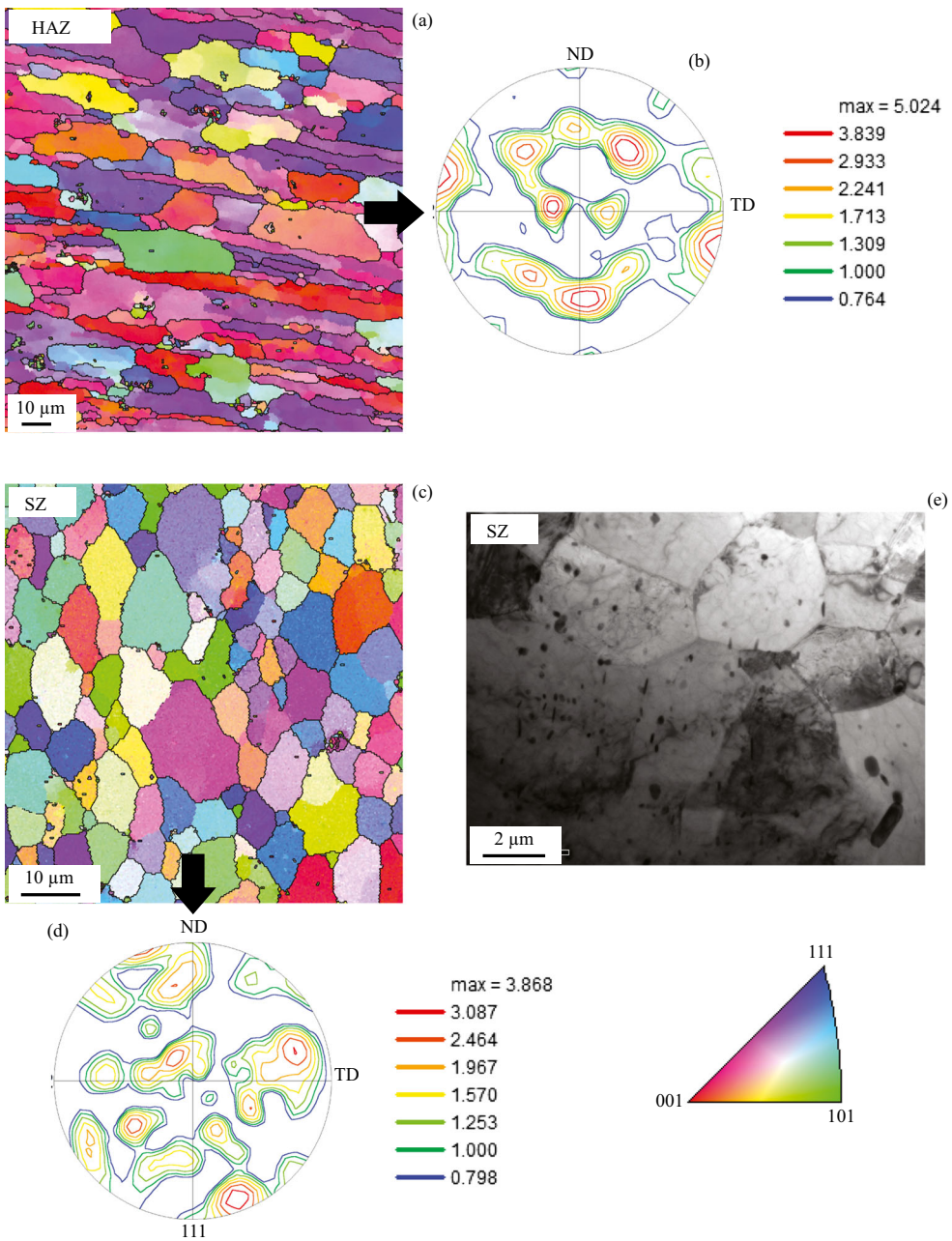

Fig. 5 EBSD orientation color maps and crystallographic textures (111 pole figure) in **a**, **b** heat-affected zone (HAZ) and in **c**, **d** stir zone (SZ), respectively, and the **e** TEM image obtained from SZ

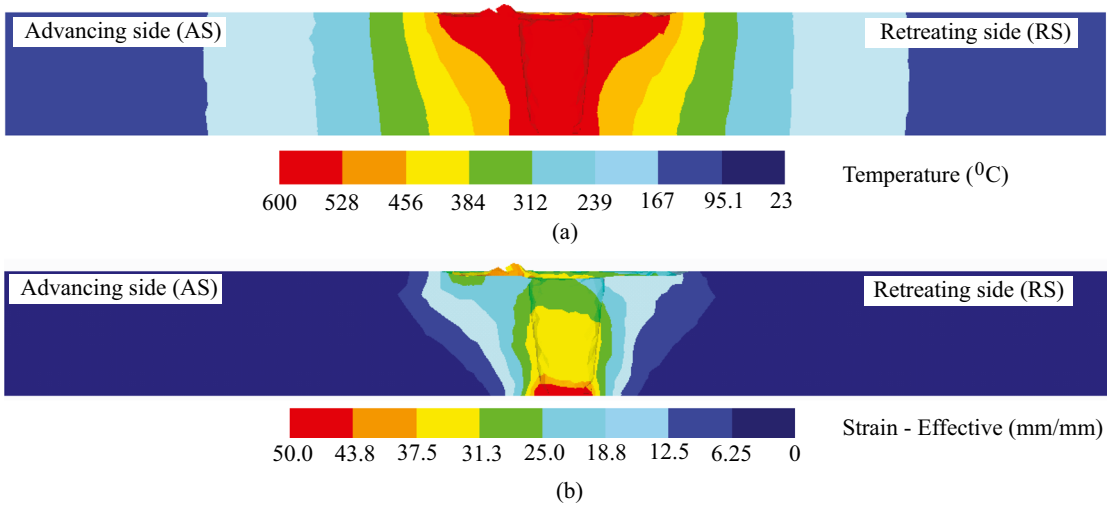

Fig. 6 **a**, **b** Temperature and strain distributions in the weld cross-section

(site saturated recrystallization). As a result, fine, equiaxed grain structure may develop as can be seen from TEM image shown in Fig. 5e.

The temperature and effective strain distribution in the transverse cross-section of the weld is shown in Fig. 6a, b. It can be seen that the temperature and effective strain distribution on the advancing and retreating sides is not symmetrical, being higher and wider on the advancing side than on the retreating side. It has been reported that the asymmetrical distribution of the velocity gradient leads to higher deformation on the advancing side as compared to retreating side. Consequently, the peak temperature is higher on the advancing side. Furthermore, the decrease in peak temperature and effective strain from top to bottom of the weld is observed as illustrated from Fig. 6a, b. It is worth noting that the combined effect of strain and temperature

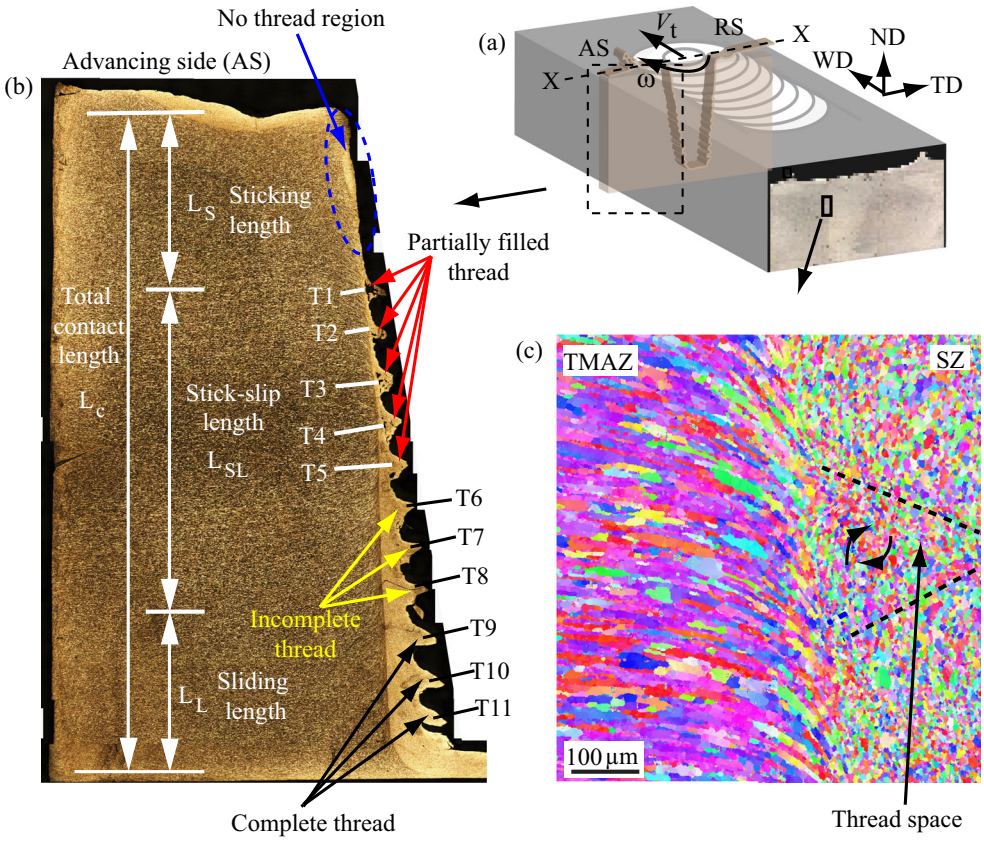

Fig. 7 **a**, **b** Optical micrographs of the weld cross-section and weld key-hole on the advancing side and **c** EBSD orientation color map showing the material deformation within the thread space in the no-thread region. Note that L_C and L_S, L_{SL}, L_L represent the total length of the contact region and the sticking, stick-slip, and sliding lengths, respectively. Also note that a thread space is defined as a space between the upper and lower flanks, bound by the root, the flanks, and the corresponding crests of the thread

results in a beneficial effect for the mechanical performance of the FSW joints due to more refined microstructure in the SZ. During the FSW process, the uppermost area of SZ is directly stirred by the tool shoulder and hence experiences severe plastic deformation at elevated temperature and strain. On the other hand, the backing plate at the bottom of the weld acts like a heat sink, producing the higher cooling rate at the bottom of the weld. Therefore, the microstructural gradient through thickness could be experienced. Figure 7 shows macrograph of the weld cross-section (see Fig. 7a), a macrograph of a key-hole section on the advancing side showing the absence and presence of thread-filled material (see Fig. 7b) and EBSD inverse pole figure map obtained across the SZ/TMAZ boundary on the advancing side (see Fig. 7c). It can be seen from this figure that the key-hole section left by the tool probe on the advancing side provides interesting information regarding the material deformation at the tool/workpiece interface. The information regarding the material filling the thread space in the no-thread region can be obtained from the EBSD orientation color map shown in Fig. 7c. It can be clearly seen from this figure that the material showed an apparent vortex motion within the thread space rather than the large-scale vertical motion. As the probe rotates, the material extruded in the thread

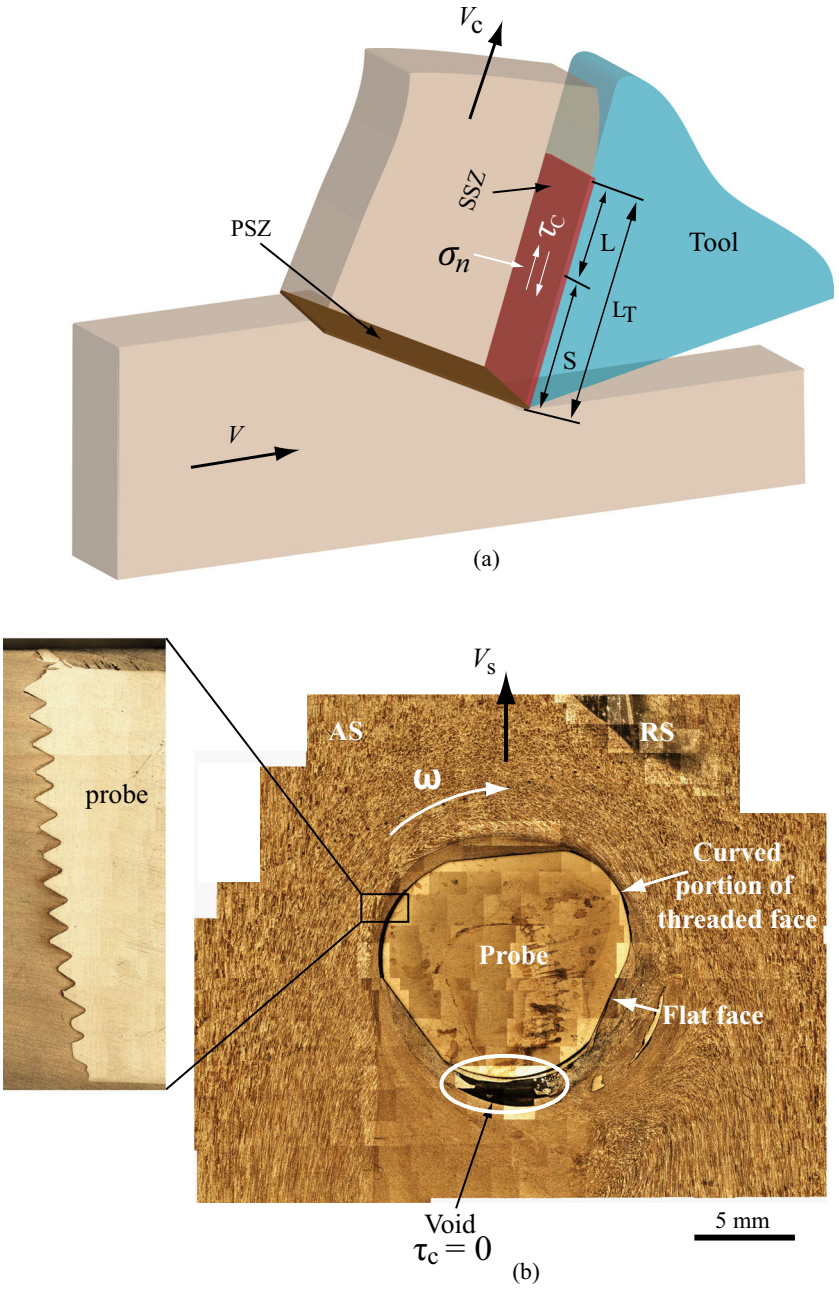

Fig. 8 **a** Schematic illustration of the material deformation in a typical metal cutting process and **b** overview of the material deformation around the Triflat^{TM} design FSW tool. Note that the material filling the thread space along weld thickness on advancing side is also shown as insert in this figure

space is sheared and forged downward by the upper flank (screwing effect). The downward forged material receives the thrust force by the lower flank. As a result, the vortex material motion within the thread space is established. Imam et al. [18] reported that the plasticized material at the thread portion of the tool probe experiences a significant downward vertical movement within the rotational zone, and hence, it helps in-process material transfer from top to the bottom. The high-velocity zone, which exists inside the thread space, causes circular flow pattern around the threaded pin (this effect can also be seen from Fig. 7c). The presence of the localized high material velocity induces significant increase in the strain rate with little change on the temperature. It is further believed that the local condition within the thread space may affect the Zener-Hollomon parameter [18, 19],

$$Z = \dot{\epsilon}\exp(\frac{Q}{\mathrm{RT}}) \tag{4}$$

where Q is the activation energy, $\dot{\epsilon}$ is the strain rate, R is the universal gas constant, and T is the deformation temperature. Therefore, employing the pin threads could be an important approach to tune the Zener-Hollomon parameter, so that control on the development of grain structure as well as resulting crystallographic textures could be achieved.

Looking from top to bottom, the appearance of the first thread T1 material starts at about one-fourth of the thickness (Ls). The progressive filling of the material in the thread space increases from T1 to T5. The threads T6–T8 are distorted upward by the upper flank of the tool, while the thread segments are separated from each other at the lower flank as can be seen in the case of thread T8. The threads T9–T11 in the bottom portion are fully developed. Based on these observations, it can be confirmed that the nature of the contact at the tool/workpiece interface significantly varies along the thickness of the weld.

To develop a fundamental understanding of the interface contact state, the flow of the plasticized material over the probe surface during the steady-state FSW operation is compared to the chip flow over the tool rake face in a typical metal cutting process of the metallic materials. This analogy can be considered by the following important reasons: (i) the contact state depends upon the shear phenomena found in both the cases; (ii) the nature of contact mainly depends upon the distribution of the stresses and peak temperatures. Three contact regimes, such as fully sticking, an intermediate contact alternating between sticking and sliding, and a sliding contact are common, and (iii) the flow pattern during the FSW can be treated as analogous to the chip formation in the metal cutting process, just as the chip morphology changes with the increasing cutting speed (V), the flow pattern in the FSW changes with the weld pitch (defined as the ratio of welding speed to tool rotational speed, $\alpha = V_s/\omega$) and tool probe shape. However, it is important to note that during the FSW, the deformed material did not escape but forced to flow all around the probe and create a bond in the trailing side of the weld. The schematic of a typical machining process with primary (PSZ) and secondary (SSZ) shear zones are shown in Fig. 8a. As the tool performs the cutting action, a large amount of heat is generated in the PSZ due to the plastic work done at the shear plane. The local heating in this zone results in the rise of the deformation temperature. This increase in the deformation temperature decreases the flow stress ($\overline{\sigma}$) of a material by the effect of thermal softening. The stress state of the material in the primary deformation zone is identified as the shear-compression stress state. At the secondary deformation zone, heat is generated due to the plastic deformation and the friction between the tool and chip. The secondary deformation zone consists of sticking (S) and sliding (L) regions. In the sticking region, the workpiece material adheres to the tool and plastic deformation occurs within the chip. On similar lines, in FSW, the material in the front of the tool is under the shear-compression stress state just as in the case of the primary shear zone in the metal cutting process. The friction between the rotating probe and the workpiece material results in a high contact shear stress (τ_c) on the workpiece material. As a result, the flow stress decreases due to increase in the deformation temperature. Figure 8b provides more details of the material deformation around the tool probe. The presence of typical geometrical features (threads and flats) of the Triflat^{TM} FSW tool can be seen in this figure (see the insert shown in Fig. 8b). The material filling in the thread space in the weld cross-section along the weld thickness is also shown in this figure. The presence of voids in the trailing side suggests that the probe/workpiece adhesive strength is not sufficiently high. Therefore, the material gets mechanically detached from the forward moving probe ($\tau_c = 0$).

A more general friction law reported by Molinari et al. [24], connecting the different contact state transitions in the FSW process could be related to the metal cutting process as follows:

$$\tau_{\mathrm{c}} = \frac{\sigma}{\sqrt{3}}(1 - e^{\mu.\sigma_{\mathrm{n}}.\sqrt{3}/\sigma}) \tag{5}$$

where μ is the sliding friction coefficient, τ_c and σ_n are the contact shear and the normal stresses, respectively. In Eq (1), it should be noted that the condition for the plastic flow occurs when $\sigma = \sqrt{3}\tau_y$, with τ_y being the shear flow stress of a material, which is a function of the temperature, strain and strain rate. For high values of σ_n, Eq (5) reduced to $\tau_c = \tau_y$ (stick-slip contact condition) and for lower values of σ_n, the Eq (5) reduces to the form, τ_c

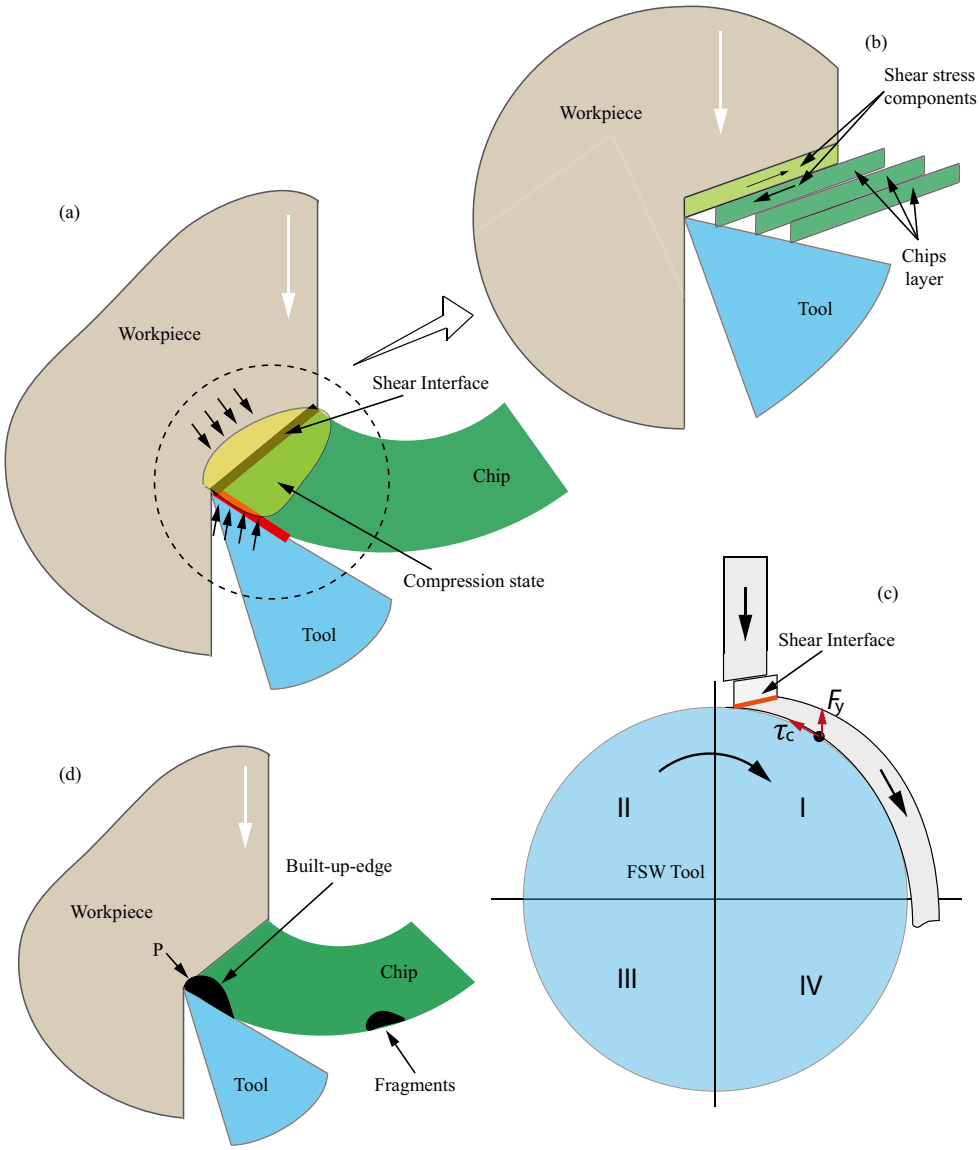

Fig. 9 **a**–**e** Comparison of material flow fields in a typical metal cutting and FSW process

$= \mu\sigma_n$. Thus, the law offers a smooth transition from the stick-clip contact state to the sliding contact state when σ_n varies. It is further important to note that shear interface in the metal cutting is an example of localized shear. At high shear strain rates, shearing is no longer homogeneous but concentrates in localized shear bands. With the rise of local temperature, local slip will be easier, and hence, local shear rate increases. This increase in local shear rate may further increase the local temperature, which is sufficient to cause the slip to occur. As a result, slip concentrates on a localized plane. Referring to Fig. 9a, b, it can be understood that because of high compression state, shear stress develops in different direction and of different magnitudes. When shear stress reaches or exceeds the shear strength of the material, the separation of chips takes place in the layer-by-layer process. On the similar line, the tool probe in the FSW process appears to be surrounded by a shear interface that corresponds to the shear interface in metal cutting process (see Fig. 9c). Furthermore, at the tool/chip interface because of rubbing action both the temperature and stress reaches a maximum value, which favors the adhesion of the tool with the chip. This phenomenon in metal cutting process is commonly referred as "build-up-edge" (see Fig. 9d). Note that with the further growth of the "build-up-edge," the resistive force (P) increases. If the force "P" exceeds the bond strength of the "build-up-edge," the separation occurs. Thus, it is believed that in the no-thread region, the contact shear stress reaches a value of the order of the adhesive force. The tool/material interface approaches the sticking contact state. Consequently, there is a direct adhesion of the plasticized material to the tool surface and removed by the tool during the termination stage.

A simple schematic showing the formation of regular 111 tetrahedrons and shear stress during FSW is shown in

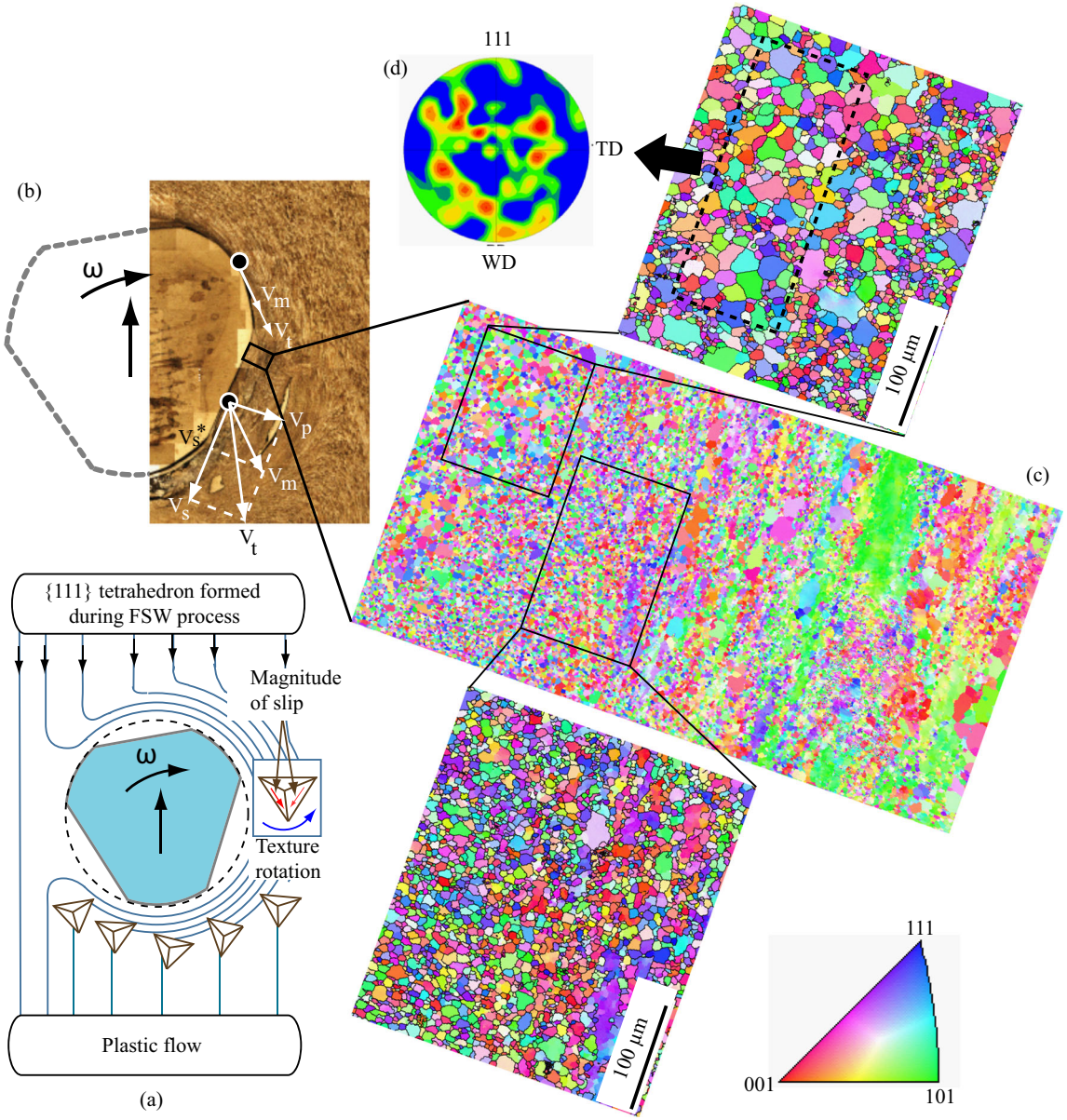

Fig. 10 **a** Schematic illustration to explain the formation of 111 pole figure, **b** velocity boundary conditions on the curve and flat portions of the Triflat^{TM} designed FSW tool, **c** EBSD orientation color map showing the diffused nugget/TMAZ boundary formed during FSW process, and **d** 111 pole figure corresponding to the selected band shown in EBSD map

Fig. 10a. In FSW, in the dominating probe region as the surface contact exists between tool probe and material, the rotation of the plasticized material depends upon the tool geometrical features. In the present case, the tool probe has a typical threads and flats, which are intentionally designed to accelerate the plastic flow within the locus of the geometrical effect of the tool probe. It is important to note that the material ahead of the tool are rotated, compressed, and sheared in the same sense as the probe rotation. The plastic flow close to the tool probe/workpiece interface experiences the severe hot deformation conditions. Both the strain rate and deformation temperatures are higher and can be connected to the fluid viscosity by using Perzyna's viscoplasticity model, $\mu = \overline{\sigma}/3\dot{\overline{\epsilon}}$ (for details see the work reported by Nandan et al. [4]), where $\overline{\sigma}$ is temperature dependent flow stress and $\dot{\overline{\epsilon}}$ is the effective strain rate. The fluid viscosity decreases significantly with both strain rate and temperature away from the tool probe axis. No significant flow occurs when the viscosity is very high. In a previous reported work by Morita and Yamanaka [32], it has been suggested that the rotation of crystallographic texture in terms of 111 pole figure occurred only around the ND

axis along the outside of the probe and can be related to the velocity distribution of plastic flow generated in the radial direction of the probe. As a result, material velocity gradient exists moving away from the tool axis causing difference in shear stress distributions within a unit volume, as shown in Fig. 10a. Furthermore, considering the partial stick-slip condition at the mid of the tool probe/workpiece interface, as shown in Fig. 10b, the material velocity (v_m) on the arc side is given by $\vec{v}_m = \gamma\ \vec{v}_t$, where, γ is slip rate and v_t is tool velocity. Moreover, the material velocity boundary condition on the flat face is given by $\vec{v}_m = \vec{v}_s^* + \vec{v}_t^* = \gamma.\vec{v}_s + \gamma\ \vec{v}_v$, where v_s and v_v are the tool velocities in parallel and perpendicular directions of the interface. It is believed that the extruded material from ahead of the tool undergoes the complex interacting flows due to the presence of threads and flats and experiences more than one rotation. It should, however, be noted that the material interaction with the flat face meets the second flow of material past the probe thread on the retreating side (for details, see the work reported by Prangnell and Heason [33]). As a result, there is much more diffused border between the nugget and TMAZ is observed, as can be seen from the EBSD orientation color map shown in Fig. 10c. The presence of bimodal grain structure, that is, equiaxed fine grains along with the slightly coarse grain structure is observed. In Fig. 10d, 111 pole figure is shown, obtained from selected orientation band taken from the accompanying EBSD map shown in Fig. 10c. Interestingly, a random crystallographic texture is observed in the selected band shown in Fig. 10c. The detailed clarification on the formation of random texture is mentioned in the discussion of the Fig. 12.

Figure 11 shows a schematic representation of the extruded workpiece material filling the thread space and high-resolution macrographs of the T1–T4, T8, and T9

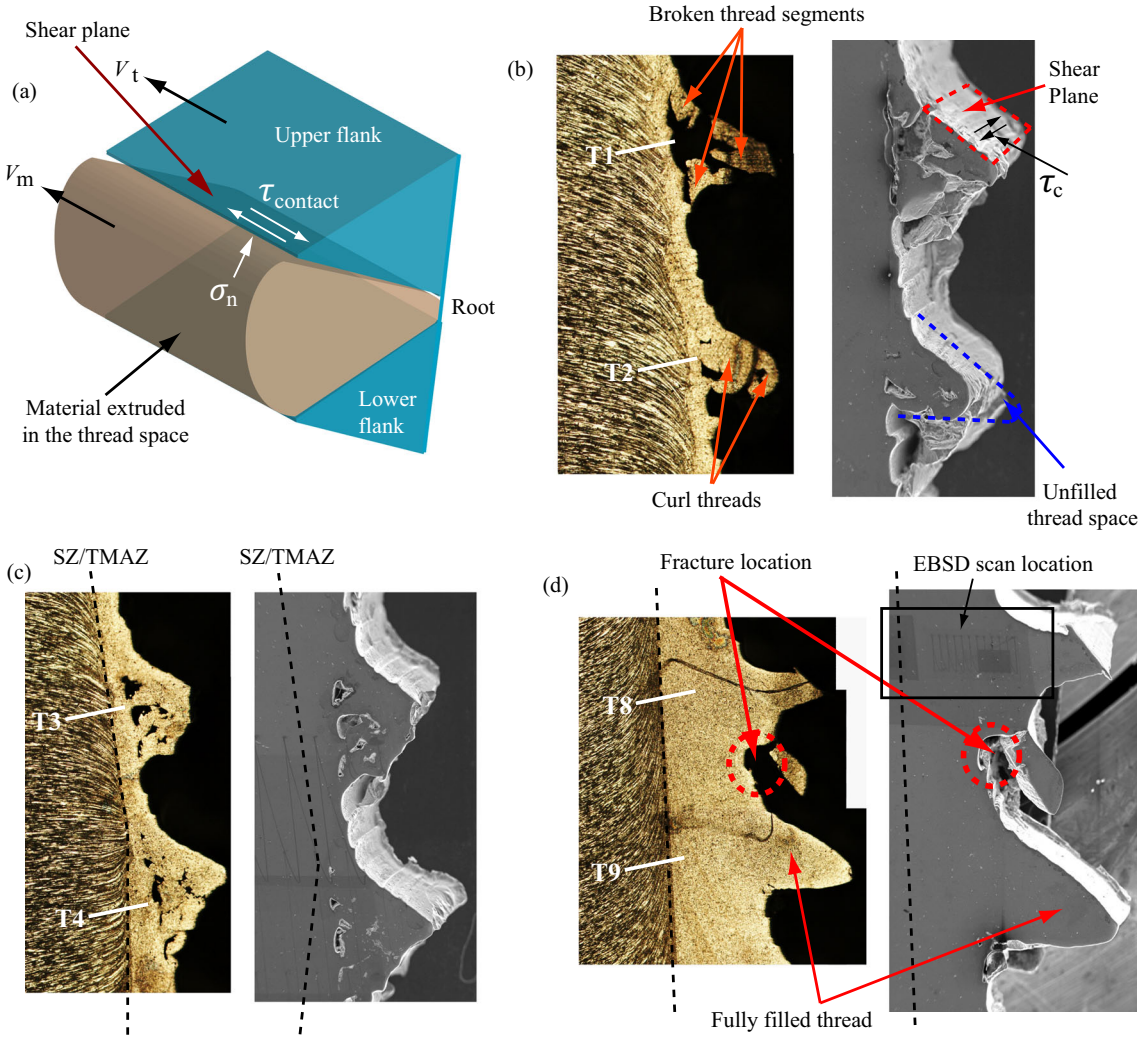

Fig. 11 **a** Schematic illustration of the material extruded in the thread space and **b–d** magnified views of the thread material morphologies along weld thickness

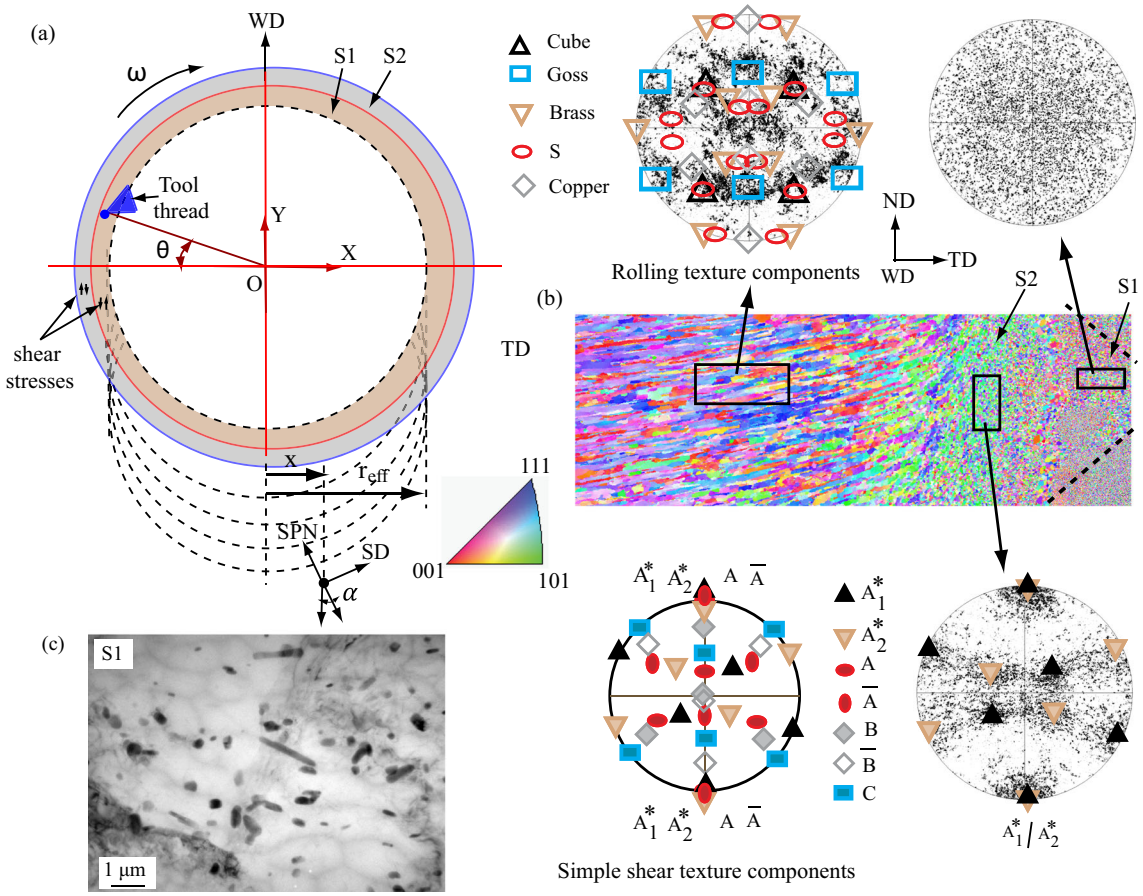

Fig. 12 **a** Schematic illustration of the plan view showing the formation of two different shear layers (S1 and S2), **b** EBSD orientation color map corresponding to the EBSD scan area shown in Fig. 11d, and **c** TEM image obtained from shear layer S1 region. Note that the crystallographic textures in the shear layers S1 and S2 and TMAZ are also shown in this figure

threads. Referring to Figs. 7b and 11b, c, the partial filling of the thread material implies that the material within the thread space may alternate between plastic flow and frictional slippage, resulting in stick-slip oscillations. The amplitude of the stick-slip oscillations decreases along the weld thickness due to increase in flow stress of the material. Consequently, the tendency of material filling the thread space increases. However, it is important to note that the magnitude of the shear stresses at the upper and lower flanks is not the same. This leads to the different plastic strain values at the upper and lower shear planes. The separation of the thread segments shown in Fig. 11d is believed from a higher plastic strain value at the lower flank leading to the shear fracture of the thread segments. The complete formation of the thread T9 in Fig. 11d and the threads T9–T11 in Fig. 7b indicates that the material filling the thread space is not rotating with the tool but is sliding against the rotating thread surface. Under such a situation, the shear flow stress of a material is sufficiently higher than the contact shear stress ($\tau_y > \tau_c$). Furthermore, an additional progressive increase of material layer outside the thread space is observed along the weld thickness (Figs. 7b and 11d). It is important to note that the material in the thread space is extruded faster than the material outside the thread space, causing the material to experience different deformation state. As a result, plastic flow of a material results in the formation of two different regions, shear layers S1 and S2, respectively. Figure 12a shows schematic illustration of the material flow in the shear layers (S1 and S2) around the probe. Note that this schematic illustration corresponds to the material flow near the thread T10 (See Figs. 7b and 11d). Here, the material passing within the thread space formed the shear layer S1 and the material in the shear layer S2 is in between the S1 and SZ/TMAZ transition layer. The effect of different deformation state in the shear layers S1 and S2 is confirmed by the different mechanisms of the grain structure formation and the corresponding crystallographic textures. Note that the local shear coordinate system, i.e., shear direction (SD), the shear plane normal (SPN), and the rotation axis (RA)

rotates with the position around the tool, this variation can be expressed by α (see Fig. 12a), which is defined by the following equation,

$$\alpha = \sin^{-1}(x/r_{\text{eff}}) \tag{6}$$

In the present case, the guideline provided by the Fonda et al. [34] is followed to obtain the crystallographic textures in the weld cross-section. The crystallographic textures in the form of 111 pole figures are shown in Fig. 12b. Fonda et al. [35] reported that there is a gradual increase in the shear strain from the shear layer S2 to S1. This gradual increase in the shear strain is reflected in the progression of the shear texture components from $\overline{A}$, A_1^* and A_2^* to C and then to a B/$\overline{B}$ component in friction stir welding of aluminum alloys, reported by Fonda et al. [34]. In addition, Shen et al. [36] reported that the B/$\overline{B}$ texture is dominant at a minimum shear strain of 20 or above, while the C component is dominant at a shear strain of 10 to 16, respectively. The crystallographic texture observed in the shear layer S2 is similar to the reported work for aluminum alloys (Fonda et al. [34]). However, the presence of random texture in contrast to the strong B/$\overline{B}$ shear texture is observed in the shear layer S1. The reason for this can be understood from the TEM image shown in Fig. 12c. The distribution of the second-phase particles in the shear layer S1 is believed to be the main reason for the formation of random texture due to PSN. Two different particles distributions can be clearly seen from this TEM image. The small particles with an approximate size of 100–500 nm, while the large particles typically in the range of 0.6–2 μm, can be found

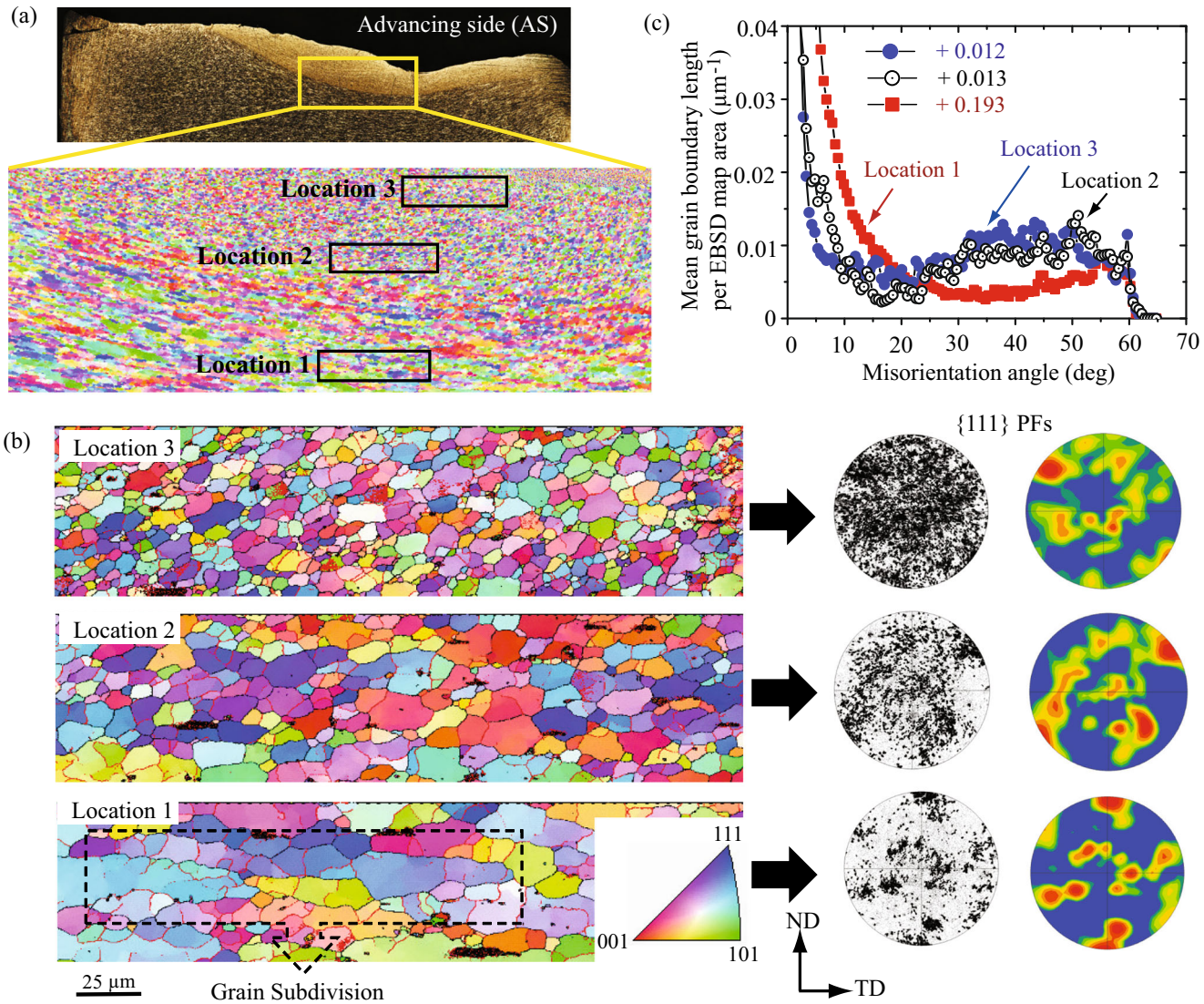

Fig. 13 **a** EBSD orientation color map on the advancing side near the top of the weld key-hole, **b** EBSD orientation color maps at locations 1, 2, and 3 and corresponding crystallographic textures, and **c** comparisons of boundary misorientation angle at locations 1, 2, and 3

from this TEM image. Thus, the retention of shear-type deformation texture in the shear layer S2 suggests that the deformation condition is dominated by the shear generated by the rotating probe, and hence, it determines the final microstructure/texture in this region.

The microstructural evolution in the weld key-hole cross-section on AS at the top of the weld is shown in Fig. 13. The enlarged view of the insert shown in Fig. 13a is represented by the EBSD orientation color map, which indicates the microstructural changes in the different weld regions. Also, the enlarged view of the locations 1, 2, and 3 are shown in Fig. 13b. Note that EBSD results are illustrated by the map colored according to the crystal orientations parallel to the sample normal direction (ND), which is indicated by the coloring in the standard stereo triangle. The black and red lines in the orientation color maps are HAGBs and low-angle grain (LAGBs) boundaries. To avoid spurious boundaries caused by the orientation noise, a lower-limit boundary misorientation cut-off of 2^o is used. The threshold angle between the high- and low-angle boundaries is 15^o. It can be seen from Fig. 13b that the grain structure shown in location 1 tends to be sheared, probably due to the geometrical requirements of the imposed strain. The microstructural evolution in this region appears to be close to the grain subdivision process. Despite the development of the grain subdivision and corresponding notable changes of the local crystallographic orientation, the crystallographic texture in the form of 111 pole figures in location 1 is still close to the shear type. With the further increase of strain from location 1 to 2, the grains are becoming more equiaxed. The textural pattern in this region tends to close to random recrystallization texture. With the further increase of strain closer to the tool shoulder/workpiece interface, the fine equiaxed grains with numerous HAGBs are formed. The mean grain boundary length per EBSD map area as a function of misorientation angles is shown in Fig. 13c. It can be seen that as compared to location 1, the significant increase in the HAGBs area is observed in location 3. Furthermore, the microstructural evolution at the bottom of the weld on AS is shown in Fig. 14. The

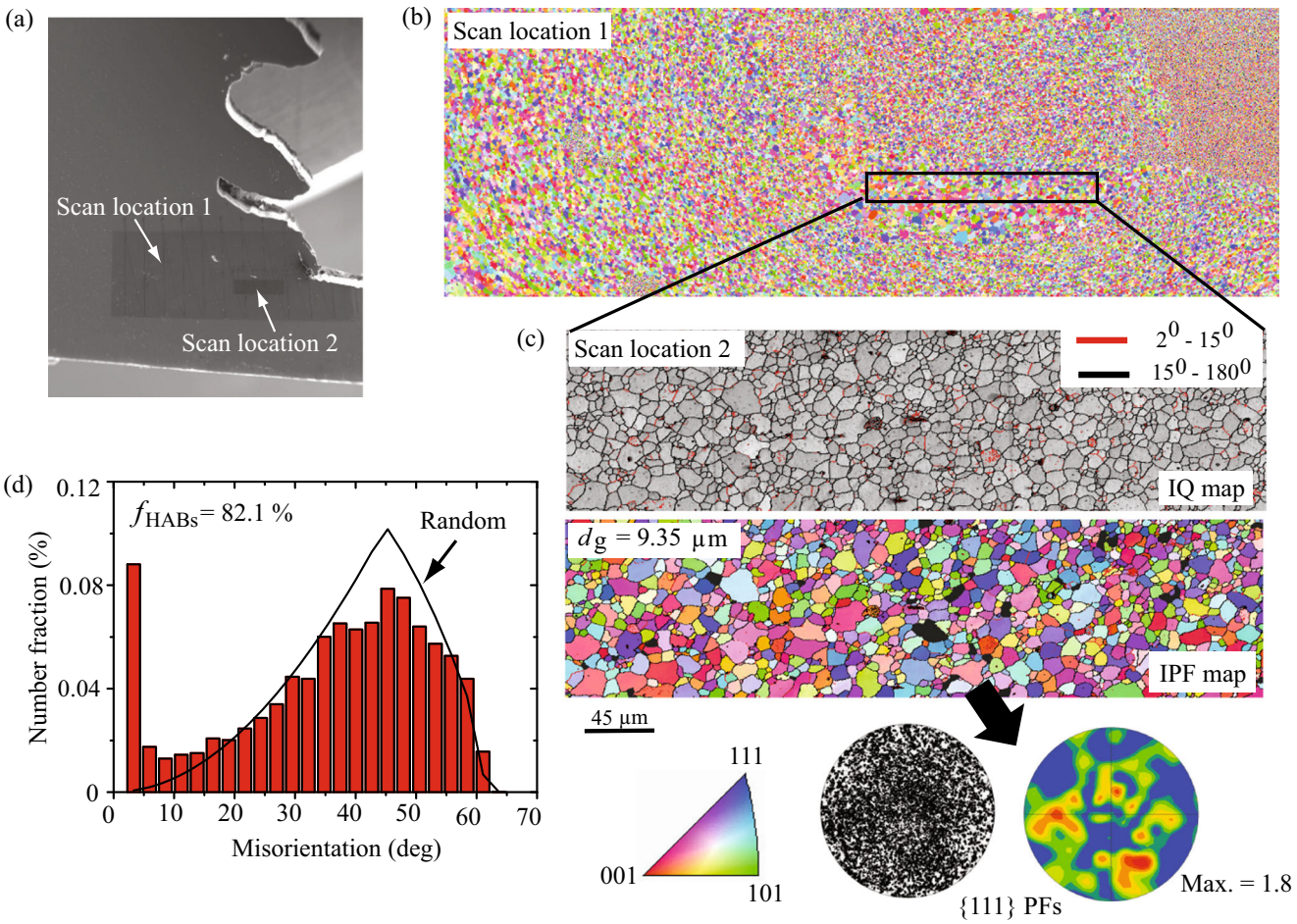

Fig. 14 **a** SEM macrograph at the bottom of weld key-hole, **b** EBSD orientation color map corresponds to scan location 1, **c** image quality (IQ) and EBSD orientation color maps correspond to the scan location 2 and the corresponding recrystallization textures, and **d** misorientation angle distribution at scan location 2

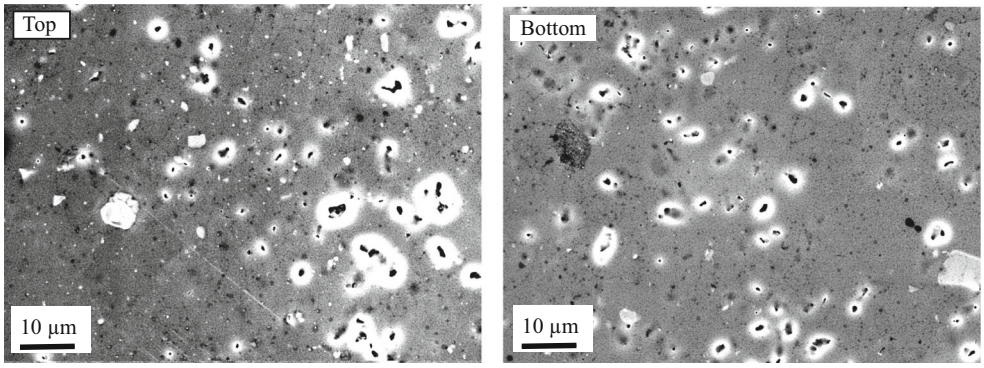

(a) (b)

Fig. 15 **a**, **b** SEM microstructures showing distribution of particles at the top and the bottom of the weld key-hole on advancing side

EBSD scan locations are shown in Fig. 14a. The EBSD orientation color map corresponding to the scan location 1 is shown in Fig. 13b. The enlarged view of the insert shown in Fig. 14b is shown in Fig. 14c. It can be seen from this figure that grains are randomly oriented as confirmed by the presence of random recrystallization texture and the HAGBs fraction is approximately equal to 82.1 % (see Fig. 14d). In particular, it has been observed that the distribution of second-phase particles plays an important role for the development of random recrystallization texture via a process called "particle stimulated nucleation" [19–23]. The distribution of particles within the SZ at the top and the bottom of the weld is shown in Fig. 15. Note that these second-phase particles are Al_6(Mn, Fe) type as confirmed from the STEM-EDS analyses conducted on these particles (for details see the previously reported work of Imam et al. [18]). It is believed that the recrystallization via PSN provides the effective nucleation sites for the development of new grains. Typically, particles must exceed a size of about 0.5 μm for PSN, reported by McNelley et al. [19]. The presence of larger particle can increase the rate of dislocation generation, and develop localized deformation zone containing large-scale misorientation gradients. This can lead to random grain orientation due to PSN, and there will be a predominance of HAGBs in the microstructure.

4 Conclusions

A cursory look at the structural performance of the FSW joints made from thicker aluminum welds shows that there exist sharp property gradients along the thickness of the weld, and hence, global stir zone properties are inferior to the base material [37]. Also, the large stresses and the high temperatures lead to wear and failure of the FSW tool. Therefore, the information presented in this work can be considered as an ideal means for the selection of tool design, importance of weld thermal management, and improving the capability of the FSW process for joining thicker plates. The following conclusions are drawn from this work:

- The weld key-hole features provide an interesting information about the nature of the contact state at the tool/workpiece interface in the case of Triflat^{TM} design FSW tool. When the contact is dominated by the stick-slip, the partial filling of the thread material started and this tendency increases along weld thickness. This particular observation implies that the material within the thread space may alternate between plastic flow and frictional slippage, promoting the stick-slip oscillations.
- A "stop-action" weld technique helps to visualize in depth the microstructural evolution in the case of Triflat^{TM} design FSW tool. The localized high-material velocities induce a significant increase in the strain rate, and thereby tune the Zener-Hollomon parameter and resulting local microstructures within thread space.
- The evidence found in the present work confirms that the PSN is the main mechanism for the grain refinement in the SZ. The homogeneous distribution of large-solute particles ($> 0.5\ \mu$m) provides effective nucleation sites for the development of new grains with random crystallographic orientation due to PSN. This leads to an increase in the HAGBs fraction, presenting an ideal condition for the superplastic behavior of the SZ material.
- At the lower portion of the weld, the complete formation of the threads is observed. It implies that the material extruded in the thread space simply slides within the thread space. The grain structure formations and the corresponding crystallographic textures in the shear layers S1 and S2 confirmed that the different deformation conditions lead to different recrystallization mechanisms in these two regions. The presence of A-type shear texture components suggests that the shear generated by the rotating probe is the main mechanism influencing the microstructure/texture

in the S2 region (closer to SZ/TMAZ interface), while, PSN is the dominant mechanism influencing the microstructure/texture in the S1 region.

The phenomenological model based on metal cutting principle offers interesting advantages for getting the insight details of deformation state in the FSW process. It provides the basis for the development of the reliable FSW models with the appropriate constitutive law and allowing researchers to evaluate the changes in the present tool design, operating parameters and possibly suggests the new improvements to the process.

Acknowledgements The authors would like to thank the staffs of the welding workshop of the Joining and Welding Research Institute of Osaka University for their cooperation and support. The authors also express their sincere thanks to Dr. Probir Saha at Indian Institute of Technology (IIT) Patna for the valuable suggestions in this work.

References

1. Imam M, Sun Y, Fujii H, Aoki Y, Ninshu MA, Tsutsumi S, Murakawa H (2017) Friction stir welding of thick aluminium welds - challenges and perspectives. Friction Stir Welding and Processing IX:119–124
2. Perrett JG, Martin J, Threadgil PL, Ahmed MMZ (2000) Recent developments in friction stir welding of thick section aluminium alloys. In: Proceedings of the 6th World Congress Al, pp 13–17
3. Mishra RS, Ma ZY (2005) Friction stir welding and processing. Mater Sci Eng R 50:1–78
4. Nandan R, DebRoy T, Bhadeshia HK (2008) Recent advances in friction-stir welding-process, weldment structure and properties. Prog Mater Sci 53:980–1023
5. Rai R, De A, Bhadeshia HK, DebRoy T (2011) Friction stir welding tools. Sci Tech Weld Join 16:325–342
6. Zhang YN, Cao X, Larose S, Wanjara P (2012) Review of tools for friction stir welding and processing. Can Metall Q 51:250–261
7. Imam M, Biswas K, Racherla V (2013) On use of weld zone temperatures for online monitoring of weld quality in friction stir welding of naturally aged aluminium alloys. Mater Des 52:730–739
8. Liu HJ, Fujii H, Maeda M, Nogi K (2003) Tensile properties and fracture locations of friction-stir-welded joints of 2017-T351 aluminum alloy. J Mater Proc Tech 142:692–696
9. Zhang Z, Zhang H (2007) Material behaviors and mechanical features in friction stir welding process. Int J Adv Manuf Technol 35:86–100
10. Zhang Z, Wu Q, Zhang HW (2016) Prediction of fatigue life of welding tool in friction stir welding of AA6061-t6. Int J Adv Manuf Technol 86:3407–3415
11. Imam M, Racherla V, Biswas K, Fujii H, Chintapenta V, Sun Y, Morisada Y (2017) Microstructure-property relation and evolution in friction stir welding of naturally aged 6063 aluminium alloy. Int J Adv Manuf Technol 91:1753–1769
12. Thomas WM, Johnson KI, Wiesner CS (2003) Friction stir welding - recent developments in tool and process technologies. Adv Eng Mater 5(7):485–490
13. Aissani M, Gachi S, Boubenider F, Benkedda Y (2010) Design and optimization of friction stir welding tool. Mater Manuf Proc 25:1199–1205
14. He X, Gu F, Ball A (2014) A review of numerical analysis of friction stir welding. Prog Mater Sci 65:1–66
15. Kuykendall K, Nelson T, Sorensen C (2013) On the selection of constitutive laws used in modeling friction stir welding. Int J Mach Tool Manuf 74:74–85
16. Garcia-Bernal MA, Mishra RS, Verma R, Hernandez-Silva D (2009) High strain rate superplasticity in continuous cast Al-Mg alloys prepared via friction stir processing. Scripta Mater 60:850–853
17. Chen Y, Ding H, Li J, Cai Z, Zhao J, Yang W (2016) Influence of multi-pass friction stir processing on the microstructureand mechanical properties of Al-5083 alloy. Mater Sci Eng A 650:281–289
18. Imam M, Sun Y, Fujii H, Ma N, Tsutsumi S, Murakawa H (2017) Microstructural characteristics and mechanical properties of friction stir welded thick 5083 aluminum alloy. Metal Mater Trans A 48:208–229
19. McNelley TR, Swaminathan S, Su JQ (2008) Recrystallization mechanisms during friction stir welding/processing of aluminum alloys. Scripta Mater 58(5):349–354
20. Zhu ZG, Sun YF, Ng FL, Goh MH, Liaw PK, Fujii H, Nguyen QB, Xu Y, Shek CH, Nai SML, Wei J (2018) Friction-stir welding of a ductile high entropy alloy: microstructural evolution and weld strength. Mater Sci Eng A 711:524–532
21. Attallah MM, Davis CL, Strangwood M (2007) Influence of base metal microstructure on microstructural development in aluminium based alloy friction stir welds. Sci Tech Weld Join 12(4):361–369
22. Oh-Ishi K, Zhilyaev AP, McNelley TR (2006) A microtexture investigation of recrystallization during friction stir processing of as-cast NiAl bronze. Metal Mater Trans A 37A:2239–2251
23. Nadammal N, Kailas SV, Szpunar J, Suwas S (2017) Microstructure and texture evolution during single- and Multiple-Pass friction stir processing of Heat-Treatable aluminum alloy 2024. Metal Mater Trans A 48A:4247–4261
24. Molinari A, Cheriguene R, Miguelez H (2012) Contact variables and thermal effects at the tool-chip interface in orthogonal cutting. Int J Solid Struc 49(26):3774–3796
25. Guerra M, Schmidt C, McClure JC, Murr LE, Nunes AC (2002) Flow patterns during friction stir welding. Mater Charact 49(2):95–101
26. Svensson LE, Karlsson L, Larsson H, Karlsson B, Fazzini M, Karlsson J (2000) Microstructure and mechanical properties of friction stir welded aluminium alloys with special reference to AA 5083 and AA 6082 5(5):285–296
27. Sato YS, Seung Park SHC, Kokawa H (2001) Microstructural factors governing hardness in friction-stir welds of solid-solution-hardened Al alloys. Metal Mater Trans A 32(12):3033–3042
28. Cahoon JR, Broughton WH, Kutzak AR (1971) The determination of yield strength from hardness measurements. Metal Mater Trans A 2(7):1979–1983
29. Vetrano JS, Bruemmer SM, Pawlowski LM, Robertson IM (1997) Influence of the particle size on recrystallization and grain growth in Al-Mg-X alloys. Mater Sci Eng A 238:101–107
30. McQueen HJ, Ryan ND (2002) Constitutive analysis in hot working. Mater Sci Eng A 322:43–63
31. Chan HM, Humphreys FJ (1984) Effect of particle stimulated nucleation on orientation of recrystallized grains. Metal Science 18:527–529
32. Morita T, Yamanaka M (2014) Microstructural evolution and mechanical properties of friction-stir-welded Al-Mg-Si joint. Mater Sci Eng A 595:196–204

33. Prangnell PB, Heason CP (2005) Grain structure formation during friction stir welding observed by the 'stop action technique'. Act Mater 53:3179–3192
34. Fonda RW, Bingert JF (2007) Texture variations in an aluminum friction stir weld. Scripta Mater 57(11):1052–1055
35. Fonda R, Reynolds A, Feng CR, Knipling K, Rowenhorst D (2013) Material flow in friction stir welds. Metal Mater Trans A 44A:337–344
36. Shen J, Wang F, Suhuddin UF, Hu S, Li W, Dos Santos JF (2015) Crystallographic texture in bobbin tool friction-stir-welded aluminum. Metal. Mater Trans A 46(7):2809–2813
37. Huang Y, Xie Y, Meng X, Lv Z, Cao J (2018) Numerical design of high depth-to-width ratio friction stir welding. J Mater Proc Tech 252:233–241